Article

Typhoon Early Warning and Monitoring Based on the Comprehensive Characteristics of Oceanic and Ionospheric Echoes from HFSWR: The Case of Typhoon Muifa

Menghua Jiang [1], Yonggang Ji [1,2,*] , Ruozhao Qu [1], Hao Zhang [1] and Jianqiang Du [1]

1   College of Oceanography and Space Informatics, China University of Petroleum (East China), Qingdao 266580, China; b23160005@s.upc.edu.cn (M.J.); b22160010@s.upc.edu.cn (R.Q.); s21160010@s.upc.edu.cn (H.Z.); z23160083@s.upc.edu.cn (J.D.)

2   Technology Innovation Center for Maritime Silk Road Marine Resources and Environment Networked Observation, Ministry of Natural Resources, Qingdao 266580, China

*   Correspondence: jiyonggang@upc.edu.cn

Abstract: As devastating natural disasters, typhoons pose a tremendous threat to human society, making effective typhoon early warning and monitoring crucial. To address this challenge, High Frequency Surface Wave Radar (HFSWR), which can observe oceanic parameters such as typhoon wind fields in real time and even capture the dynamic changes in the ionosphere, has become an effective tool for typhoon monitoring. This paper investigates the interaction mechanisms about Typhoon-Acoustic Gravity Waves (AGWs)-Ionosphere, as well as Typhoon-Ocean Waves for HFSWR, and simulates these interaction processes within HFSWR. Then a typhoon early warning and monitoring scheme for HFSWR has been proposed: In the first stage, the S-shaped ionospheric disturbances observed by HFSWR are utilized as precursor signals for early typhoon warnings. In addition, the second stage involves analyzing changes in first-order oceanic echo spectral peak ratio to pinpoint when the typhoon eye enters the radar detection range, thus initiating the typhoon monitoring phase. Subsequently, the measured data from HFSWR collected during Typhoon "Muifa" (2212) in conjunction with the proposed scheme are evaluated in detail. The results indicate that AGWs generated by typhoons can propagate into non-typhoon areas within the detection range, causing S- shaped ionospheric disturbances and providing approximately 6 h of early warning. At around 8:05 (UTC+8), an increasing trend in the first-order spectral peak ratio was noted, indicating the entry of the typhoon eye into the detection range, which closely aligns with the official typhoon path and marks the transition to the monitoring phase. The proposed scheme is expected to enhance the capability for typhoon early warning and real-time monitoring in specific sea areas and mitigate the risks associated with typhoon-related disasters.

Keywords: HFSWR; typhoon early warning and monitoring; acoustic gravity waves; ionospheric echoes; oceanic echoes

1. Introduction

Typhoons are highly destructive tropical cyclones that can bring intense storms, torrential rain, and massive waves, causing severe natural disasters. As a result, it is crucial to monitor typhoons in real time and issue early warnings. Currently, typhoon monitoring methods mostly comprise numerical prediction systems, meteorological satellites, GNSS, etc. Due to its unique all-weather and over-the-horizon detection capabilities, High Frequency Surface Wave Radar (HFSWR) demonstrates notable advantages in typhoon monitoring, particularly its ability to maintain stable operation under severe typhoon conditions and provide dual observation of oceanic and ionospheric parameters.

Typhoons can cause dramatic changes in the ocean surface, and numerous scholars have analyzed oceanic dynamic parameters monitored by HFSWR during typhoon periods [1–4]. For instance, Lai et al. successfully observed the wind direction changes during

Typhoon "Songda" (1102) using three SeaSonde systems, which verified the effectiveness of HFSWR in observing typhoon wind directions [5]. Li et al. detected the Typhoon "Chan-hom" (1509), showing that HFSWR can also reflect the wind field distribution [6]. Furthermore, Xu et al. used the vortex field structure extracted by HFSWR to determine the real-time position of the typhoon eye and obtained the trajectory through continuous observations, which was almost consistent with the optimal typhoon path released by the China Meteorological Administration (CMA) [7]. Zhou et al. further found that the wave field rotation center captured by HFSWR always appeared in the left area of the optimal typhoon path, providing an important reference for typhoon path prediction [8]. Xie et al. analyzed the overall performance and applicable conditions of HFSWR in inverting ocean currents, ocean waves, and wind fields about Typhoon "Ampil" (1810), verifying that HF-SWR still has good detection capabilities under complex sea conditions [9]. These studies fully demonstrate the wide application and significant achievements of HFSWR in typhoon monitoring, including offshore typhoon parameter characteristics, typhoon eyes, typhoon paths, and other aspects.

It is worth noting that typhoons can also exert a significant impact on the ionosphere. Specifically, during typhoon activities, the phenomenon of Traveling Ionospheric Disturbances (TIDs) often occurs [10]. As early as 1958, Bauer discovered through ionospheric sounding equipment that the f0F2 showed an increasing trend before the arrival of hurricanes [11]. Later, Shen et al. further confirmed the correlation between typhoons and f0F2 [12]. Xiao et al. collected 24 typhoon records and found that there were almost always mesoscale TIDs, and strong typhoons could cause the Doppler frequency shift waveform to take an "S" shape [13]. At the same time, typhoons can also affect the interaction between the ionosphere and HFSWR. For example, Li et al. verified the feasibility of using HFSWR ionospheric characteristics for typhoon monitoring by calculating the SNR of ionospheric echoes [14]. Chung et al. conducted a detailed analysis of the impact of typhoons on ionospheric echoes based on the Range Doppler (RD) spectrum obtained by HFSWR. They found that the proportion of banded clutter increased significantly as the typhoon approached [15]. These findings offer robust evidence supporting the utilization of HFSWR to capture ionospheric disturbances for typhoon monitoring.

Regarding the reasons why typhoons can cause TIDs, Hines et al. proposed using the theory of acoustic gravity waves (AGWs) to explain the changing patterns [16]. AGWs, as a stable periodic atmospheric disturbance, typically have periods ranging from several minutes to several hours [17]. The AGWs excited by typhoons often result in mesoscale TIDs, with horizontal scales between 100 and 200 km. Numerous studies have shown that HFSWR possesses the capability to capture TID information and observe AGWs that trigger these disturbances. For instance, Zhou et al. used the OSMAR to observe that TIDs, generated by AGWs, caused amplitude fluctuations of approximately 0.6 Hz in the F2 layer [18] and also noted the morphology when multiple S-shaped time-frequency components were superimposed [19]. By simulating the time frequency distribution (TFD) of the ionospheric echo spectrum, Chen et al. analyzed the impact of TIDs on Doppler frequency shifts [20]. Lyu et al. monitored Typhoon Rumbia (1818) by HFSWR and confirmed that the S-shaped Doppler frequency shifts were due to AGWs [21]. Furthermore, several researchers have further investigated the chaotic dynamic characteristics of ionospheric echoes [22–24], leveraging the distinctive features of HFSWR ionospheric echoes recorded during typhoon occurrences, which provides new theoretical support for early warning of typhoons and other sudden sea conditions using HFSWR.

In recent years, while numerous scholars have utilized HFSWR to study oceanic echoes, ionospheric echoes, and AGWs in the context of typhoons, most of these efforts have focused on typhoon monitoring. There has been limited exploration into the application of these findings specifically for early typhoon warnings in specific sea areas. Addressing this gap, this paper proposes a novel typhoon early warning and monitoring scheme that leverages the comprehensive characteristics of oceanic and ionospheric echoes. We achieve this by analyzing the intricate interactions among Typhoon-AGWs-Ionosphere

and Typhoon-Ocean Waves as observed through HFSWR. By conducting an in-depth investigation of radar data collected during Typhoon Muifa, we scrutinize the changes in oceanic and ionospheric echoes before and after the typhoon entered the radar detection range, assessing the feasibility of our proposed scheme. The primary contributions of this paper are as follows:

(1)   We present simulation results of ionospheric and oceanic echo spectra observed by HFSWR before and after the passage of a typhoon, highlighting the interaction processes among Typhoon-AGWs-Ionosphere and Typhoon-Ocean Waves. These results can provide compelling evidence for the utility of TIDs in typhoon early warning efforts.

(2)   By synthesizing the distinct characteristics of ionospheric and oceanic echoes observed before and after typhoon passage, we propose a comprehensive early warning and monitoring scheme tailored for HFSWR. This scheme is designed to enhance the proactive response to sudden marine conditions, such as typhoons, using new-generation surface wave radar.

(3)   The practical feasibility of the proposed scheme is validated using measured data collected during Typhoon Muifa.

The remainder of this paper is organized as follows: Section 2 delves into the analysis and simulation of the coupled processes involving Typhoon-AGWs-Ionosphere and Typhoon-Ocean Waves as detected by HFSWR. Section 3 introduces a typhoon early warning and monitoring scheme employing HFSWR. Section 4 provides a detailed analysis of the measured data obtained during Typhoon Muifa. Eventually, Section 5 summarizes the conclusion.

2. Typhoon-Ocean Waves and Typhoon-AGWs-Ionosphere Coupled Mechanisms for HFSWR

Under typhoon conditions, HFSWR achieves concurrent observations of oceanic and ionospheric echoes. This is due to the fact that typhoons not only have a substantial impact on oceanic dynamic parameters, but also trigger the upward transmission of AGWs into the ionosphere, altering its characteristics. In addition, HFSWR can accurately capture these reactions. Figure 1 illustrates the interactions between HFSWR and ocean waves, as well as HFSWR and ionosphere under a typhoon.
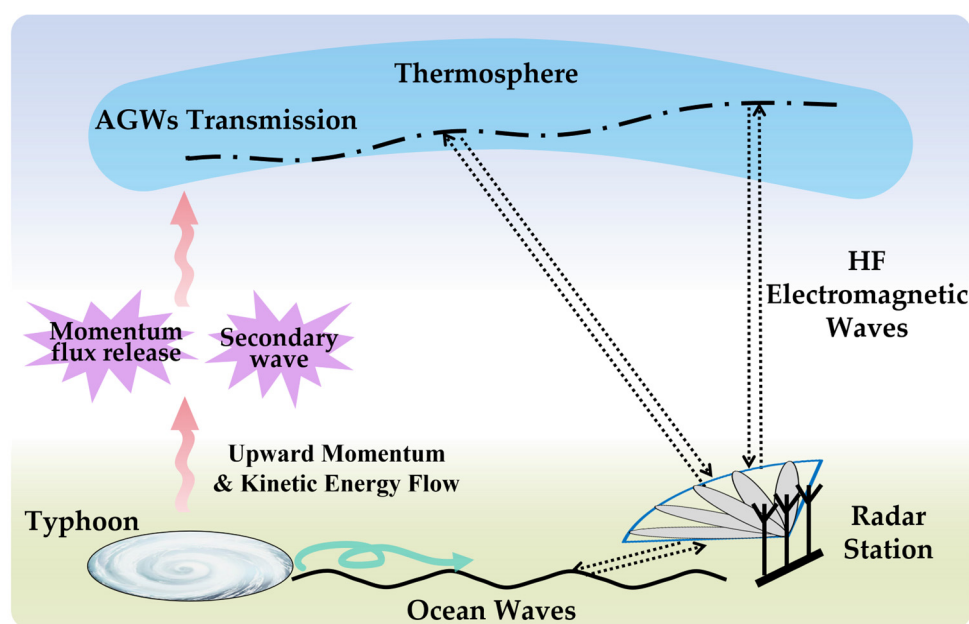
Figure 1. Schematic diagram of the interactions between HFSWR and ocean waves, as well as HFSWR and ionosphere during a typhoon period.

During typhoon activities, high frequency (HF) electromagnetic waves can resonate with two distinct rows of first-order ocean waves via Bragg scattering, one moving towards the radar and the other moving away, which will produce the positive and negative first-order oceanic echoes. Notably, the typhoon wind direction is highly related to the ratio of the two first-order peaks of the oceanic echoes [25]. In addition, the rotating wind direction is a distinctive feature of a typhoon. As a result, when using HFSWR to monitor a typhoon, the ratio will change significantly as the typhoon evolves. According to the research [26], if a typhoon originates from the left of a radar station, an increasing ratio can serve as an indicator that the typhoon eye is approaching the radar detection range. Furthermore, when the ratio transitions from negative to positive values, it definitely signifies that the typhoon eye has fully entered the detection range, which can offer a novel perspective for typhoon monitoring.

Concurrently, typhoons can also induce the AGWs, which result in an upward transfer of kinetic energy and momentum across the atmospheric layers. Owing to the upward density gradients, wave propagation leads to variations in amplitude within the atmosphere. Near the mesosphere, these amplitude variations may lead the waves to a critical state, causing them to rupture and generate secondary waves upon releasing momentum fluxes [27]. In this process, the AGWs propagate along complex pathways to the ionosphere, carrying energy and momentum that stimulate the movement of neutral atmospheric particles. Then, these particles collide with the charged ions in the ionosphere, leading to fluctuations in electron density, known as TIDs. The changes in ionospheric electron density induce nonlinear phase path alterations of HF electromagnetic waves, ultimately causing a Doppler shift in the HFSWR ionospheric echo spectrum.

2.1. Coupled Mathematical Models

This section will provide a detailed elaboration on the coupled models previously mentioned, specifically the Typhoon-Ocean Waves and Typhoon-AGWs-Ionosphere coupled processes for HFSWR. In addition, the latter will be explained in three parts: the process of typhoons exciting AGWs, the process of AGWs inducing TIDs and the interaction between TIDs and HFSWR.

On the one hand, we employ the first-order scattering cross section [28], namely Equation (1), which is constructed using the JONSWAP wave spectrum [29] and the cardioid wind direction function [30] to model the HFSWR first-order oceanic echo spectrum.

$$\sigma_1(\omega) = 2^6 \pi k_0^4 \sum_{m=\pm 1} S(-2mk_0) \cdot \delta\left(\omega - m\sqrt{2gk_0}\right) \tag{1}$$

where ω represents the Doppler frequency, k_0 denotes the Bragg wave number, S stands for the directional sea wave spectrum, $m = \pm 1$ signifies the positive and negative first-order spectral peaks, and g is the gravitational constant.

Additionally, to elucidate the variations in wind direction and the relationship between the typhoon and radar detection range, we utilize Equation (2) to calculate the first-order spectral peak ratio.

$$R = 10\log_{10}\left(\frac{\sigma_1(\omega)}{\sigma_1(-\omega)}\right) \tag{2}$$

where $\sigma_1(\omega)$ and $\sigma_1(-\omega)$ denote the positive and negative first-order scattering cross section.

On the other hand, with respect to how typhoons affect the ionosphere as reflected in the HFSWR ionospheric echo spectrum, first of all, we model the process of typhoons exciting AGWs with the compressible Navier-Stokes equations, similar to [31,32]. The atmospheric momentum, energy, and continuity equations are involved in this process,

and they can be utilized to determine the wave equation of AGWs, which can be calculated as follows:

$$\frac{\partial^2 \vec{W}}{\partial t^2} = \frac{1}{\rho}\nabla(\gamma p \nabla \cdot \vec{W}) - \frac{\nabla p}{\rho}\nabla \cdot (\rho \vec{W}) + \frac{1}{\rho}\nabla(\vec{W} \cdot \nabla)p$$
$$+ \frac{\partial}{\partial t}\left(\nu_1 \nabla^2 \vec{W} + \left(\nu_2 + \frac{\nu_1}{3}\right)\nabla(\nabla \cdot \vec{W})\right) - \frac{\partial}{\partial t}(\vec{W} \cdot \nabla \vec{W}) \tag{3}$$

where $\vec{W}$ denotes the velocity of AGWs, p, ρ, and T represent atmospheric pressure, mass density, and temperature, respectively. ν_1 and ν_2 stand for the first and second kinematic viscosities, and γ is the adiabatic index. It not only reveals the mechanism of typhoons exciting AGWs but also lays the foundation for further analysis of the impact of AGWs on the ionosphere.

Secondly, we explore how AGWs trigger TIDs [32,33], which can be solved through the following magnetohydrodynamic equations.

$$\frac{\partial \vec{v}_s}{\partial t} = \frac{q_s}{m_s}\left(\vec{E} + \vec{v}_s \times \vec{B}_o\right) - f_s\vec{v}_s + f_s\vec{W} \tag{4}$$

$$\vec{J} = \underline{\sigma} \cdot \vec{E} + \vec{J}_w; \vec{J}_w = e\left(n_i\vec{v}_i - n_e\vec{v}_e\right) \tag{5}$$

$$\frac{\partial n_s}{\partial t} + \nabla \cdot \left(n_s\vec{v}_s\right) = P - L \tag{6}$$

$$\nabla^2\vec{E} - \nabla\left(\nabla \cdot \vec{E}\right) - \frac{1}{c^2}\frac{\partial^2\vec{E}}{\partial t^2} - \mu_o\frac{\partial\vec{J}}{\partial t} = 0 \tag{7}$$

$$\nabla^2\vec{B} - \frac{1}{c^2}\frac{\partial^2\vec{B}}{\partial t^2} = -\mu_o\nabla \times \vec{J} \tag{8}$$

where $\vec{v}_s$, n_s and f_s denote the velocity, number density of fluid s, and frequency of collision between s and neutral (s can be i or e, signifying ions and electrons. $q_i = +e$, $q_s = -e$). $\vec{E}$, $\vec{B}$ and $\vec{J}$ stand for the fluctuating electric field, magnetic field, and net current of the ionosphere. $\vec{B}_o$ is the Earth's magnetic field, $\underline{\sigma}$ is the ionospheric conductivity tensor, and $\vec{J}_w$ is the current density induced by the AGWs. P, L are the production and loss of ions and electrons by photo ionization and chemical reactions, respectively. c and μ_o represent the speed of light in a vacuum and the magnetic susceptibility. Equations (3)–(8) constitute a closed set of solutions, which can be numerically resolved using the finite difference method and temporally integrated with the implicit Crank–Nicholson method. Notably, $\vec{W}$ Equation (4), specifically relating to the winds associated with AGWs, can drive ionospheric currents and directly depends on the outcome of Equation (3), which can effectively link the first two processes via this parameter.

Thirdly, we elaborate on the interaction between TIDs and HFSWR. Numerous studies have yet to reach a consensus regarding the propagation path of ionospheric echoes detected by HFSWR, and in most cases, the intensity of vertically reflected ionospheric echoes often exceeds that of mixed-path propagation [18]. Moreover, typhoons can significantly affect the F-layer of the ionosphere [34,35], with F-layer echoes most likely originating from the vertical direction [36]. Thus, this part employs the received power in the Doppler dimension of the FMCW signals based on the third-order spectral density model of vertical irregularities [37], as shown in Equation (9).

$$P(\omega_d) = \frac{k_0^3 \eta_0 \Delta l^2 I_0^2 A_r \sin^2(\Delta\theta)}{32\pi^4 R_0^2 \Delta\varphi^4} \times \left| \int_0^{\Delta\varphi} J_0\left(\frac{\omega_d - 2k_0 v_v}{v_h}\varphi\right)\varphi d\varphi \right|^2$$

$$\times Sa^2(k_B R') \left\{ 1 + \frac{4z_0 r_e^2 \lambda_0^2}{k_0} \log\frac{z_0}{z_0 - z_0'} \cdot \frac{8\pi^3 k_0 \langle N_e^2 \rangle}{\sin\alpha_I \left(k_0^2 + ((\omega_d - 2k_0 v_v)/v_h)^2\right)^{3/2}} + \cdots \right\} \tag{9}$$

where ω_d, $\Delta\theta$, and α_I are the Doppler frequency, angle error of the antenna pattern of the elementary dipole, and magnetic inclination, respectively. k_0, η_0, I_0, R_0, and J_0 represent the wavenumber, intrinsic impedance of antennas, peak current, ionosphere refraction range, and zero-order Bessel function. φ indicates the diameter of the scattering area varied from 0 to $\Delta\varphi$, and $\Delta\varphi$ is the diameter of the ionospheric scattering spot. $k_B = 2\pi B/c$, and B represents the sweep bandwidth. $R' = R_0 - R$, and R stands for the target range. z_0 is the ionosphere thickness and z_0' is the height of below z_0 on the order of one radar wavelength. v_v and v_h denote the vertical and horizontal drift velocity, $\langle N_e^2 \rangle = C_0 n_e$ represents the variance of electron density fluctuations, where C_0 and n_e are the fluctuation coefficient and electron density. Notably, the variations in v_v, v_h, and n_e are derived from solving the magnetohydrodynamic equations in the second part. By plugging these parameters into Equation (9), we can obtain the HFSWR ionospheric echo spectrum under typhoon influence, thereby establishing an effective link between the second and third parts.

2.2. Simulation Results

Building upon the foundational models outlined in Section 2.1, this section will delve into the corresponding simulation results of the coupled processes involving Typhoon-Ocean Waves and Typhoon-AGWs-Ionosphere for HFSWR.

Figure 2 illustrates the simulation results of wind direction and first-order oceanic echo spectrum, encompassing both one-dimensional and two-dimensional spectrum, across three phases of the typhoon: before, during, and after its passage. The first column shows the results before the typhoon, the second column during its passage, and the third column after. Notably, the one-dimensional spectrum in the third row corresponds to the two-dimensional spectrum in the second row at the range of 70 km, as indicated by the red line in Figure 2d–f. Assuming the typhoon originates from the left side of the radar detection range, as depicted in Figure 2a, the wind direction is initially directed away from the radar before the typhoon's arrival. As illustrated in Figure 2d,g, the intensity of the negative first-order Bragg peak is greater than that of the positive one during this phase. When the typhoon enters the detection range, shown in Figure 2b, its direction becomes nearly perpendicular to the radar beam, exhibiting an overall rotational trend. At this point, Figure 2e,h indicate that the intensities of the positive and negative first-order Bragg peaks become comparable. After the typhoon passes, as depicted in Figure 2c, the direction shifts towards the radar. Figure 2f,i reveal that the intensity of the positive first-order Bragg peak surpasses that of the negative one. These observations also align with established patterns of typhoon movement.

Figure 3 depicts the results of AGW propagation induced by a typhoon, and the upper parameters in the figure represent the AGWs' propagation time in the atmosphere, vertical velocity and horizontal velocity, respectively. As indicated in Table 1, we select some hydrodynamic parameters of a typical typhoon as initial conditions [38] to guarantee the broad applicability of the simulation results, with the vertical velocity serving as the initial excitation for the simulation of AGWs. At the initial time, ambient ionosphere (p, ρ, v_1, T, $\vec{W}$) can be obtained from the SAMI2 model. The results reveal that under the influence of typhoons, AGWs can reach the ionosphere within 14.92 min. Furthermore, after 40 min of propagation, the horizontal velocity of AGWs reached 5.85 m/s, which is comparable to the translational speed of the typhoon.
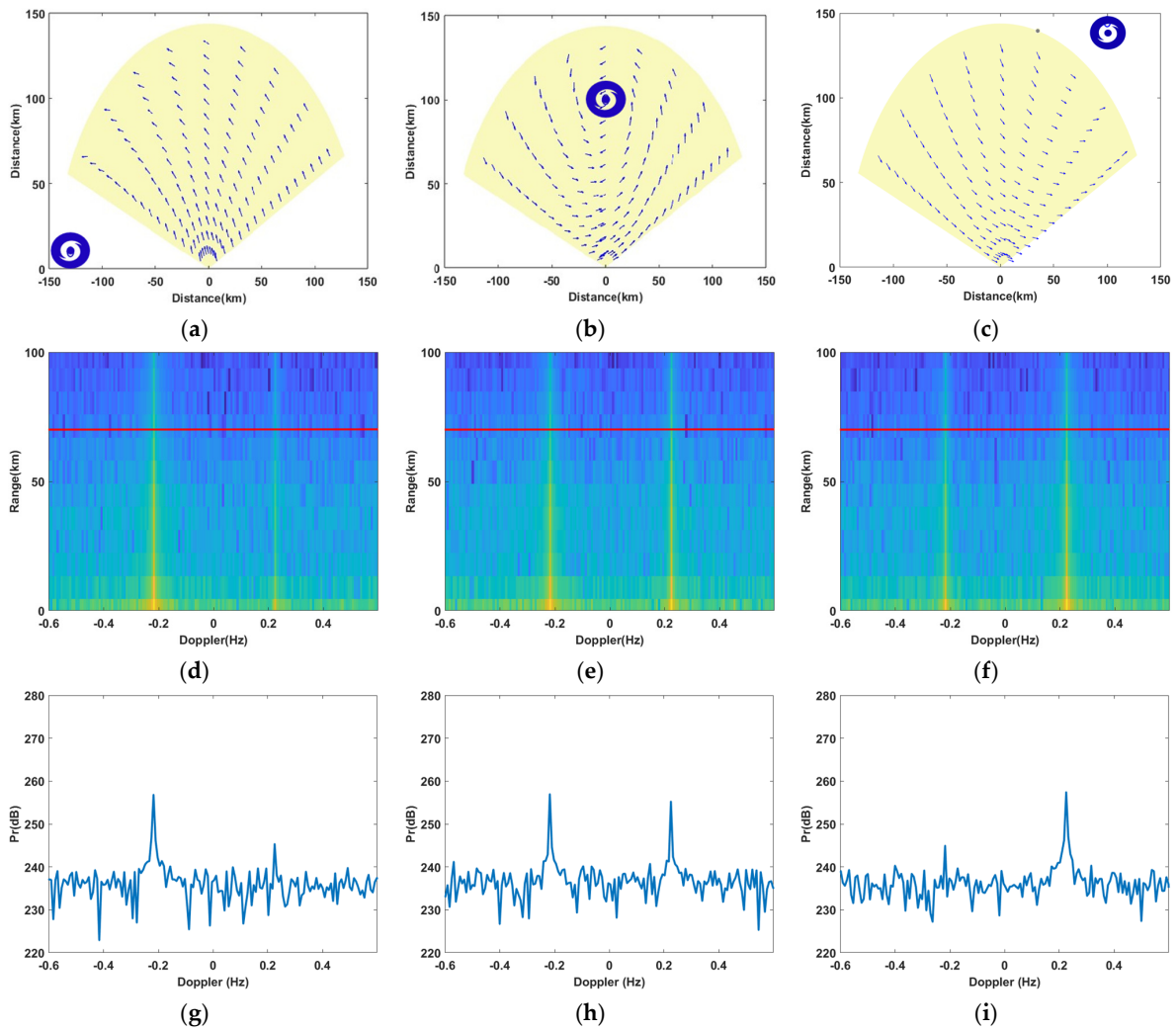
Figure 2. Simulations of wind direction and first-order oceanic echo spectra under the influence of a typhoon. (**a**–**c**) Simulations of wind direction before, during, and after the typhoon passage, respectively. (**d**–**f**) Simulations of two-dimensional spectrum before, during, and after the typhoon passage, respectively. (**g**–**i**) Simulations of one-dimensional spectrum (range = 70 km) before, during, and after the typhoon passage, respectively.
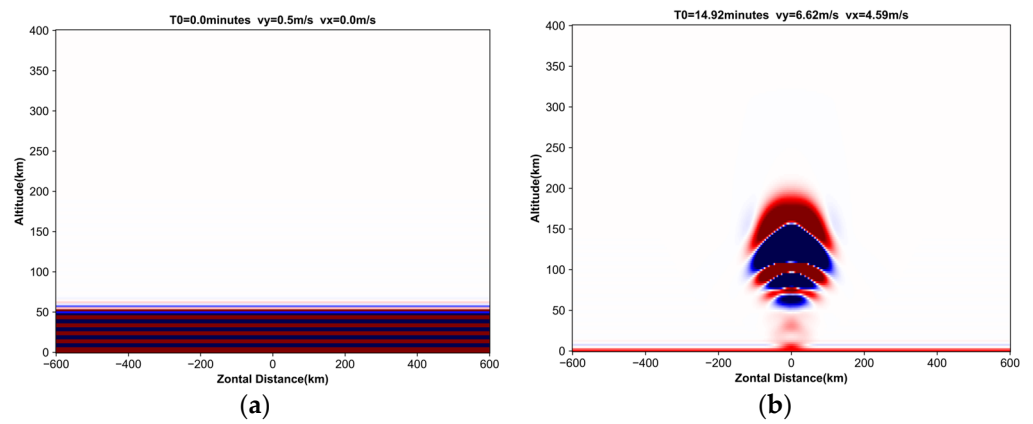
Figure 3. Simulations of the AGWs under the influence of a typhoon. (**a**) The propagation time of AGWs is 0 min. (**b**) The propagation time of AGWs is 14.92 min.

Table 1. Hydromagnetic parameters of a typical typhoon.

Parameter	Value
Vertical speed	0.5 m/s
Velocity of translational motion	5–10 m/s

Building on previous analyses, we assume that when AGWs reach the ionosphere, they will promptly interact with charged particles in the ionosphere, leading to fluctuations in electron density that are confined to one-dimensional horizontal directions. To simulate the TIDs triggered by AGWs, we apply concentric cosine waves across a horizontal distance at the ionosphere's lower boundary (set to 100 km) to replicate the effects of AGWs, as depicted in Equation (10) [39].

$$n_x = A \times \cos\left(\frac{2\pi}{\lambda}R_x - \frac{2\pi}{T}t\right) \tag{10}$$

where A denotes the amplitude of AGWs, λ and T represent the horizontal wavelength and period. R_x stands for the horizontal distance from the point of AGWs excitation, and t is time. Based on the horizontal and vertical velocity of AGWs from the first part, we can further solve for the changes in ionospheric electron density influenced by AGWs. Given that the cycles of TIDs range from tens to hundreds of minutes, we allocate a 300-min simulation period to adequately replicate the dynamic changes. T and λ are assumed to be 30 min and 100 km, respectively. Figure 4 illustrates the simulation results of TIDs influenced by AGWs. The green line depicts the contours of electron density, while the three parameters above represent the TIDs' propagation time in the ionosphere, the maximum horizontal drift velocity of ionospheric irregularities, and the average absolute value of the horizontal drift velocity. Given that the most common distance range affected by typhoons is 300–600 km, occasionally reaching 800 km or more, we set the horizontal distance (horizontal axis) to −600 km~+600 km, with ± indicating directions towards or away from the typhoon. In addition, for the ionospheric variables (i.e., n_s, $\vec{E}$, $\vec{B}$ and $\vec{J}$, their gradients in the p direction should be zero, ensuring compliance with the transmissive boundary conditions at altitudes of 100 km and 600 km. According to the calculation results of Equations (3)–(8), the average drift speed of ionospheric irregularities reached 12.92 m/s by the 22nd minute, surpassing the speed of typical typhoons, with the maximum drift speed potentially exceeding the typhoon's speed by an order of magnitude.
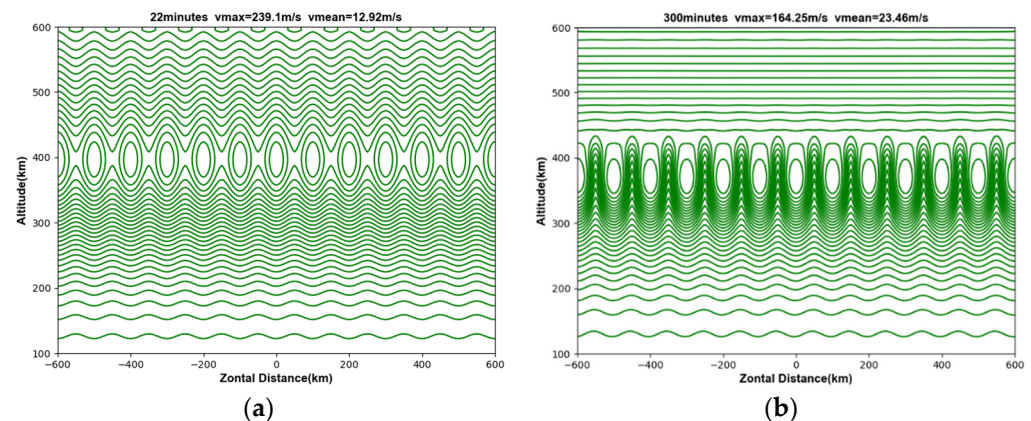
Figure 4. Simulations of the variations in electron density under the influence of AGWs. (**a**) The propagation time of TIDs is 22 min. (**b**) The propagation time of TIDs is 300 min.

Assuming the excitation point of AGWs is located at 0 km and the radar station is positioned at +600 km, where the ionosphere within the radar detection range has been perturbed. Due to the real-time movement of typhoons, the distance between the radar

station and the typhoon will vary continuously. By analyzing the temporal variations in ionospheric electron concentration and horizontal and vertical drift velocity, along with Equation (9), we can obtain the TFD results of the HFSWR ionospheric echo spectrum over this duration. Additionally, the simulated electron density in this study may be influenced by upper limit conditions. Figure 5a displays the TFD of the ionospheric echo spectrum based on the parameters in Table 1. The figure shows that the HF Doppler disturbances induced by AGWs form a distinct S-shaped pattern with a period of about 150 min, which aligns with the theoretical cycle. Moreover, ionospheric echoes are observed exclusively on the negative Doppler axis with a negative phase velocity, consistent with the downward-to-upward propagation of AGWs. To further highlight the influence of AGWs on the ionospheric echoes, we also simulate the TFD without detecting ionospheric disturbances for comparison, as depicted in Figure 5b. It is evident that the energy is more dispersed and lacks a clear S-shaped disturbance.
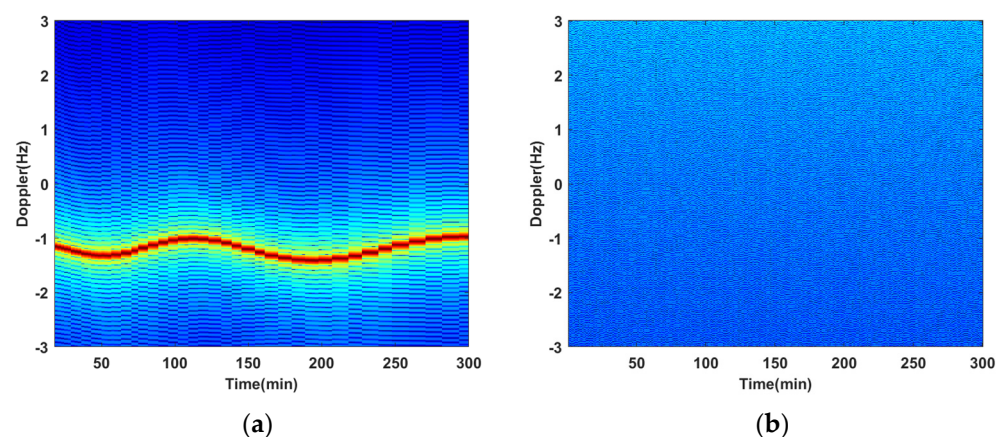
Figure 5. Simulations of TFD based on the ionospheric echo spectrum. (**a**) Simulations when the TIDs exist within the radar detection range. (**b**) Simulations when there are no TIDs within the radar detection range.

In fact, typhoons trigger the generation of AGWs, which propagate obliquely. However, for simplicity in our calculations, we neglect the horizontal propagation distance of AGWs. We define the time for AGWs to reach the ionosphere as T_0, the time for TIDs to enter the radar detection range as T_1, and the time for the radar detecting the ocean waves as T_2. If the condition $T_0 + T_1 < T_2$ is satisfied, it means that the changes in the ionosphere have been observed before the radar detects the ocean waves, which provides us with the possibility of using TIDs information for typhoon early warning. Conversely, when $T_0 + T_1 \geq T_2$, the ionospheric information obtained through HFSWR would pertain only to typhoon monitoring rather than early warning. Assuming the typhoon moves at a steady 10 m/s and the interaction time of Bragg scattering between HF electromagnetic waves and ocean waves is negligible, the typhoon's travel time can be approximated as T_2. Thus, we can calculate the straight-line distance of the typhoon's movement, denoted as S_2. Additionally, by combining the average horizontal drift velocity of the ionospheric irregularities at any given moment with the time T_1, we can derive the travel distance of the TIDs, represented as S_1. Through calculation, it is found that about 64.92 min (i.e., $T_0 + T_1$) after the excitation of AGWs, the ionospheric disturbance overtakes the typhoon, with S_2 being about 38.95 km and S_1 about 39.71 km. In other words, when the distance between the radar station and the AGWs excitation site exceeds 38.95 km or the allowed warning time exceeds 64.92 min, the TIDs caused by the typhoon can be detected by HFSWR, serving as a warning signal. While the trajectory of typhoons can be unpredictable and they do not consistently maintain a uniform speed along a straight path, they typically last for several days and are a relatively persistent system. Thus, theoretically, the TIDs observed by HFSWR can be effectively utilized to facilitate early warning for typhoons.

3. The Scheme About Typhoon Early Warning and Monitoring for HFSWR

The analysis presented in Section 2 indicates that typhoons can significantly impact the ionosphere and wind fields, which are subsequently reflected in the RD spectrum, enabling effective typhoon early warning and monitoring. On the one hand, AGWs induced by typhoons cause the TFD of ionospheric echoes to display a distinct S-shape, as illustrated in Figure 5a. This phenomenon is likely to be observed prior to the typhoon entering the radar detection range, thus offering valuable insights for early warning. On the other hand, the distribution of typhoon wind fields and the positional relationship between the wind eye and HFSWR can be discerned through the first-order spectral peak ratio of oceanic echoes, thereby facilitating real-time typhoon monitoring.

Consequently, based on the premise that typhoons can cause disturbances to the ionosphere and ocean waves, this section introduces a comprehensive scheme for typhoon early warning and real-time monitoring that integrates information of ionospheric and oceanic echoes, with a detailed flowchart of the scheme depicted in Figure 6.
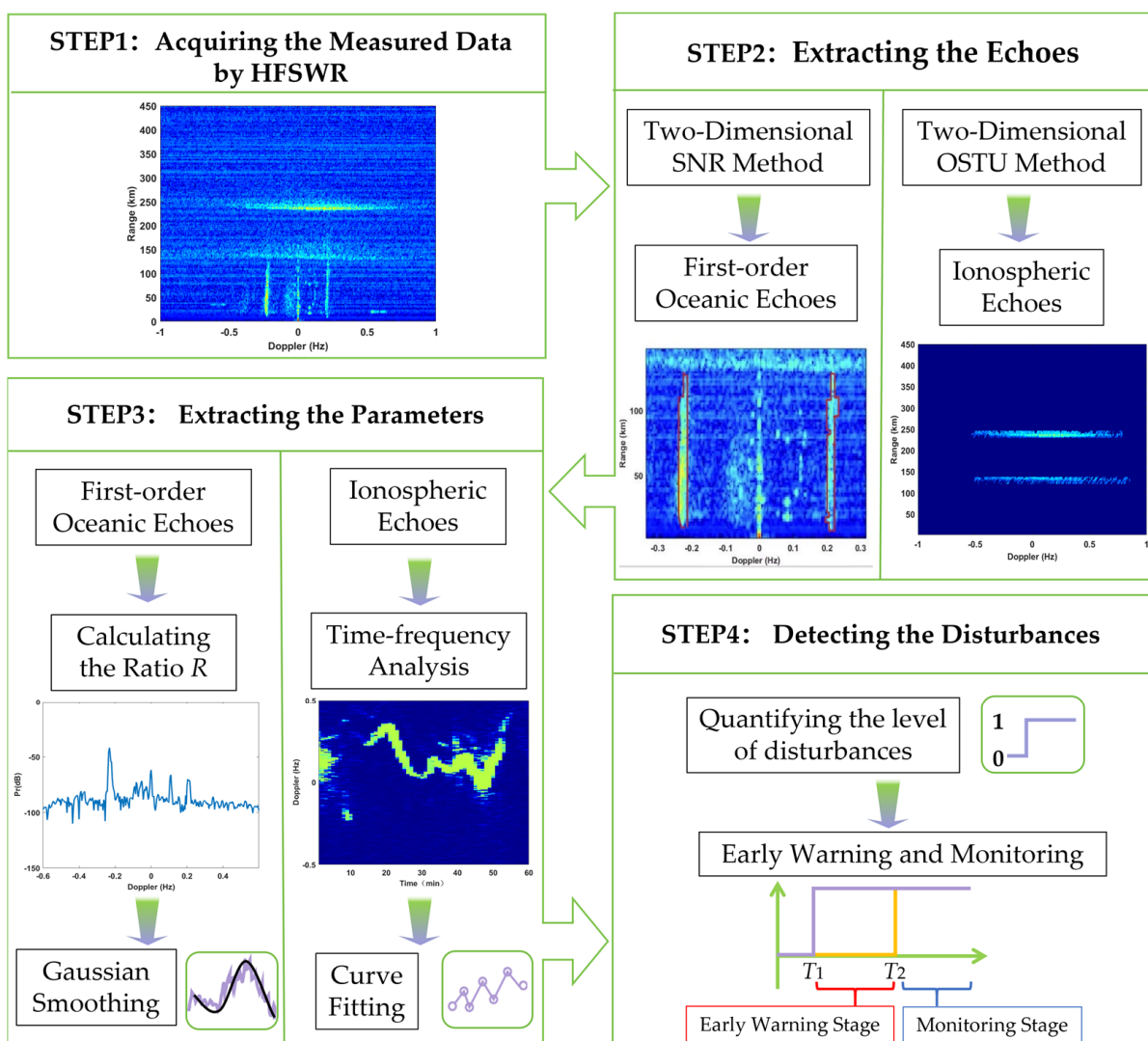
Figure 6. Flowchart for typhoon early warning and monitoring using HFSWR.

The initial step involves the acquisition of measured data using HFSWR. Following preprocessing, the received echo signals are first transformed into range domain information and then into the frequency domain via Fast Fourier Transform (FFT). To comprehensively capture the Doppler effect of the signal and the information it carries, the frequency domain

information is subsequently converted to the Doppler domain, ultimately yielding the RD spectrum. This spectrum includes critical information such as oceanic echoes resulting from the resonance of ocean waves with electromagnetic waves and ionospheric echoes formed by reflections.

The next step is the extraction of echoes within the RD spectrum. Specifically, the two-dimensional signal-to-noise ratio (2D-SNR) method [40] is employed to identify and extract the first-order oceanic echoes. This method capitalizes on the continuous distribution of first-order oceanic echoes in the distance domain, along with the higher SNR of these echoes compared to the background noise, thereby enabling more effective extraction. In addition, due to the impact of propagation loss on electromagnetic waves over longer distances, it is believed that within a range of 100 km, HFSWR is more effective in receiving signals with higher SNR, making it the optimal distance for ocean echo observation. After the extraction and removal of oceanic echoes, the Otsu algorithm [41], also known as the maximum inter-class variance method, is utilized to extract the ionospheric echoes, ensuring the accuracy and completeness of the echo information.

The subsequent step aims to extract key parameters from the echoes. For first-order oceanic echoes, Equation (2) is used to calculate the R during the observation period, followed by smoothing the results using a Gaussian filter. In addition, for ionospheric echoes, the spectrogram method is employed to obtain the TFD, and a detailed analysis of the Doppler characteristics is conducted to precisely capture the ionospheric information, including TIDs. Since the TFD results may include multiple Doppler values at a single moment, this study selects the Doppler value corresponding to the maximum echo amplitude as the sampling point and employs cubic spline interpolation to fit the results.

Finally, it is necessary to perform disturbance detection and quantification on the results. To enhance visual representation for the ionospheric TFD, the appearance of an S-shaped phenomenon indicates that the typhoon has impacted the ionosphere and resulted in TIDs. The typhoon warning phase is then initiated, and the detection result is marked as "1"; otherwise, it is marked "0". For oceanic echoes, when the onset of the typhoon eye is detected within the range of HFSWR, the result is marked "1" and enters the typhoon monitoring phase; otherwise, it is marked "0". The times when the ionospheric and oceanic echoes are marked as"1" are recorded as T_1 and T_2, respectively, with the time difference between them representing the available early warning time.

4. The Processing and Analysis of Measured Data During Typhoon Muifa

This section will delve into the effectiveness of the proposed typhoon early warning and monitoring scheme in Section 3, primarily using the measured data of typhoon Muifa recorded by the HFSWR station in Weihai, Shandong Province, from 2:00 a.m. to 15:00 p.m. (UTC+8) on 16 September 2022. The radar operates at a frequency of 4.7 MHz and scans from $-40°$ to $40°$. Typhoon Muifa, the most intense typhoon landing in China annually, has brought severe impacts on the eastern regions of both East China and Northeast China.

Figure 7 illustrates the trajectory of Typhoon Muifa as it approached the Bohai Sea. The red solid circle indicates the location of the radar station, the yellow sector indicates the radar detection range, the red line traces the typhoon path, and the blue circle delineates the extent of the typhoon wind circle. Observations reveal that the typhoon eye entered the radar detection range at around 8:00 a.m. on 16 September 2022, and exited around 12:00 p.m. Notably, the typhoon wind circle had already entered the detection range around 5:00 a.m. and exited around 3:00 p.m. Figure 8 calculates the hourly distance between the typhoon and the radar station from 2:00 a.m. to 3:00 p.m., revealing that the typhoon was closest to the radar at 8:00 a.m.
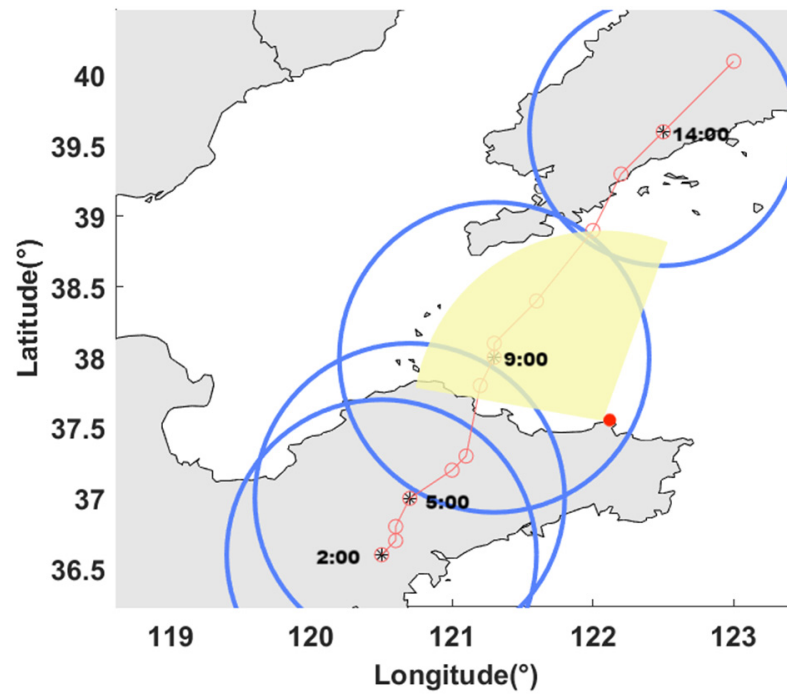
Figure 7. The path of typhoon Muifa around the Bohai Sea.
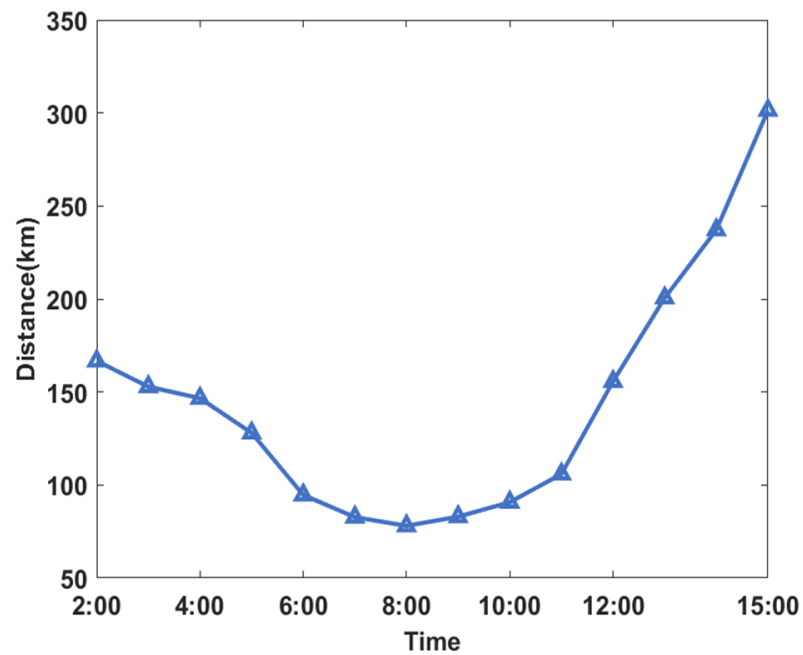
Figure 8. The distance between the typhoon and the radar station.

Since the ionosphere is frequently influenced by solar and geomagnetic activities, it is crucial to thoroughly analyze the levels of solar and geomagnetic activity during typhoons before investigating the specific effects of typhoons on the ionosphere in order to rule out potential disturbances from other factors. Consequently, this study employs the solar radiation flux F10.7 index to quantify solar activity and utilizes the equatorial geomagnetic index Dst and the global geomagnetic index Kp to assess the intensity of geomagnetic activity. Data from the NOAA revealed that the F10.7 index on that day was 131 (sfu), signifying a moderate level of solar activity. Figure 9 illustrates the variations in the Dst and Kp indices on the day of the typhoon. As can be clearly observed, the Kp index

consistently remained below 2, suggesting a period of calm in geomagnetic activity, and the Dst index also indicated stability on that day. Therefore, it can be reasonably inferred that the potential impacts of solar and geomagnetic activity on radar observations during the acquisition of measured data are minimal. If disturbances are observed in the data, they are more likely due to the AGWs induced by the typhoon.
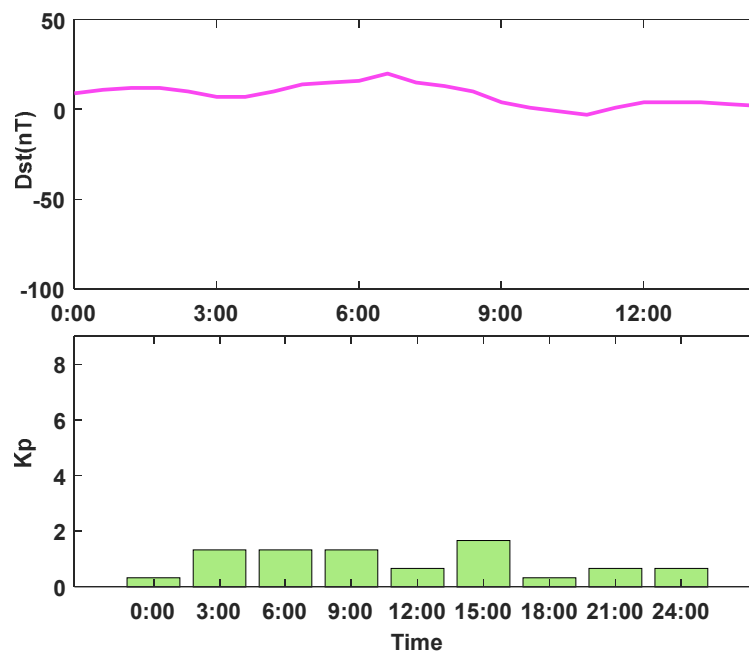
Figure 9. Geomagnetic activity on 16 September 2022.

Figure 10 displays the RD spectra collected at the Weihai HFSWR station during Typhoon Muifa, revealing significant changes in ionospheric and oceanic echo patterns as the typhoon progressed. When the typhoon had not yet entered the radar's detection range (as exemplified by Figure 10a), the main region of the ionosphere was asymmetrically distributed around 0 Hz, with substantial differences between consecutive moments. Additionally, the negative first-order sea echo significantly surpassed the positive echo in both detection range and energy. As the typhoon progressively moved into the radar's detection range, as seen in Figure 10b,c, the ionospheric echoes exhibited Doppler broadening exceeding 1 Hz, displaying an approximately symmetrical distribution centered around 0 Hz, sometimes along with longitudinal tilting. For the oceanic echoes, as the typhoon approached, the disparity between the negative and positive echo diminished. After the typhoon exited the detection range (as illustrated in Figure 10d), the main ionospheric region shifted once more, with the positive first-order oceanic echo now clearly surpassing the negative echo. These observations can enhance understanding of the complex mechanisms of interaction between typhoons and the ionospheric-oceanic system.

Figure 11 shows the TFD results based on the extracted ionospheric echoes, specifically during the period before the typhoon entered the radar detection range (from 2:00 to 6:00), with a range unit selected as 309 km. In the upper part of Figure 11a, a typical S-shaped wave can be clearly observed. It is noteworthy that similar but slightly different S-shaped fluctuations also appear in adjacent range units (Figure 11b,c), which may result from the inherent thickness and complex motion state of the ionosphere, as well as the limitations of radar resolution. To display the characteristics of TIDs more intuitively, we use the method in Step 3 of Section 3 to take the maximum echo amplitude in Figure 11a as sampling points, and fit the results using cubic spline interpolation. The fitting results are shown in the lower part of Figure 11a, where the blue circles represent the sampling points and the orange lines are the fitted curves. By comparing the TFD results with the

fitted curve, it is found that when a disturbance occurs, the amplitude of the fitted curve exhibits minor fluctuations and also exhibits an S-shape, with a clear correlation between the amplitudes at adjacent moments. Conversely, when no obvious S-shaped disturbance occurs in the TFD results, the slope of the fitted curve will undergo drastic changes. Based on these characteristics, we believe that the time when the slope does not change abruptly is the time when the ionosphere is disturbed, and the corresponding time is marked as "1". Conversely, the location of the slope change is the time when the ionosphere is not disturbed, and it is marked as "0". Given that AGWs usually have a specific period, we determine that disturbances lasting longer than 10 min are likely the TIDs triggered by the typhoon, as indicated by the red line in Figure 11a. The results of this discrimination are highly consistent with the measured data, and this method has the potential to identify TIDs in other distance units. (It has been verified that disturbances occurring around 5:30 can be observed in the ionosphere in the range of 243.75 km).
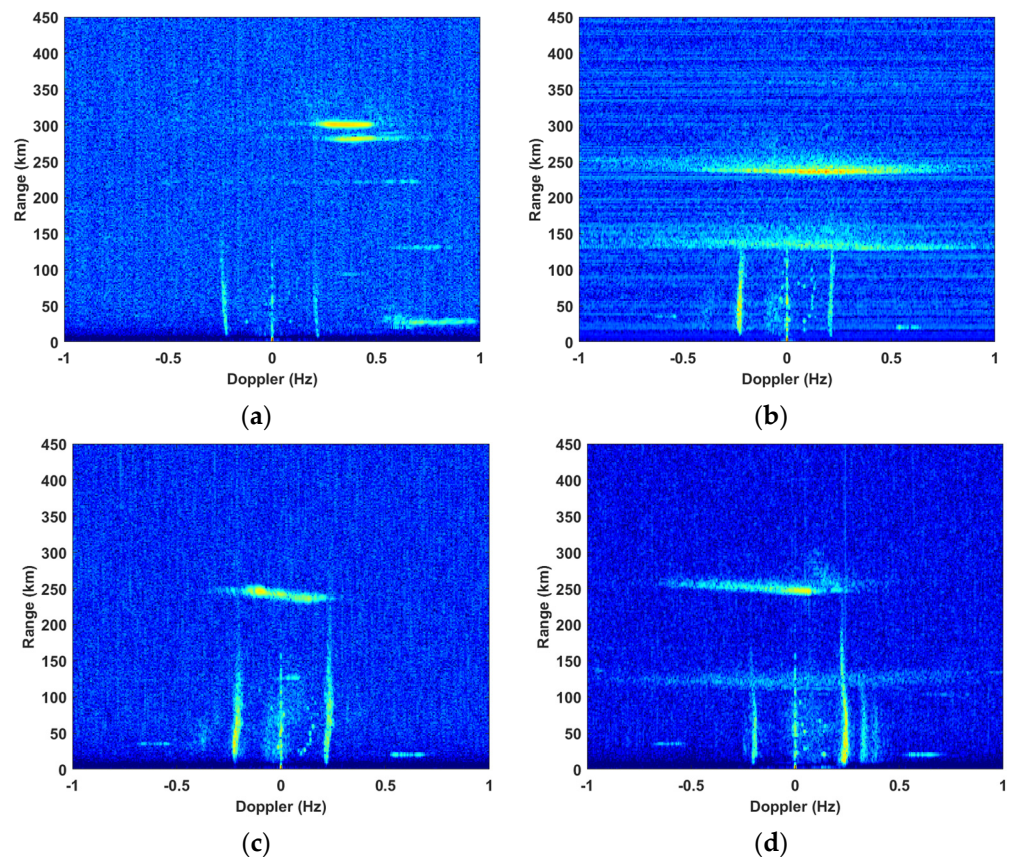
Figure 10. The RD spectra based on HFSWR. (**a**) The RD spectrum at 3:00 a.m. (**b**) The RD spectrum at 8:00 a.m. (**c**) The RD spectrum at 10:30 a.m. (**d**) The RD spectrum at 14:00 p.m.

The aforementioned method has been extended to the periods when the typhoon entered (from 6:00 to 12:00) and exited (from 12:00 to 15:00) the radar detection range. Figure 12 displays the results during the typhoon entry into the detection range. The range unit is 243.75 km, with the TFD results above and the disturbance detection results below. Figure 13 illustrates the results after the typhoon exited the detection range. The range unit is 265 km, with the TFD and disturbance detection results in the upper and lower sections, respectively. The disturbance detection results exhibit good consistency with the TFD results of HFSWR ionospheric echoes.
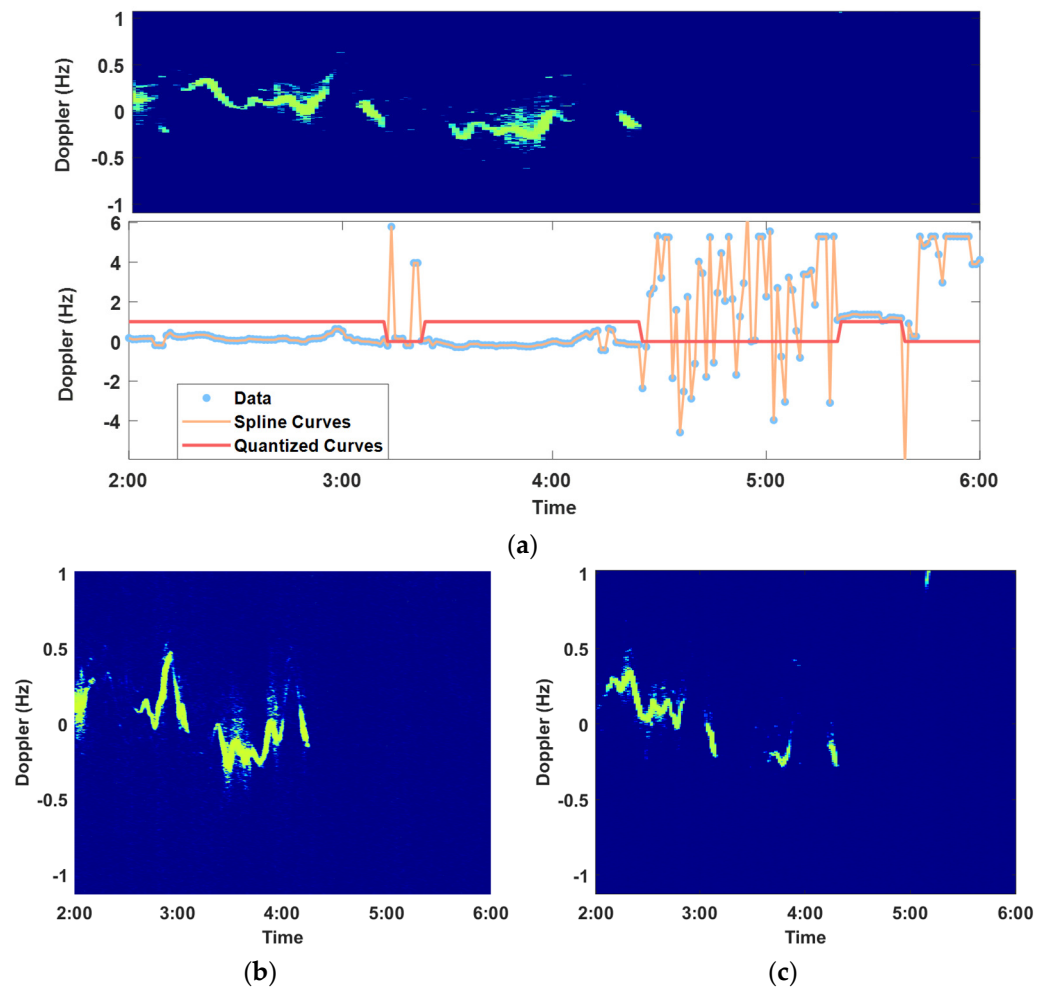
Figure 11. The results before the typhoon entered radar detection range. (**a**) Time-Doppler and disturbance detection results at 309 km. (**b**) Time-Doppler results at 305 km. (**c**) Time-Doppler results at 311 km.
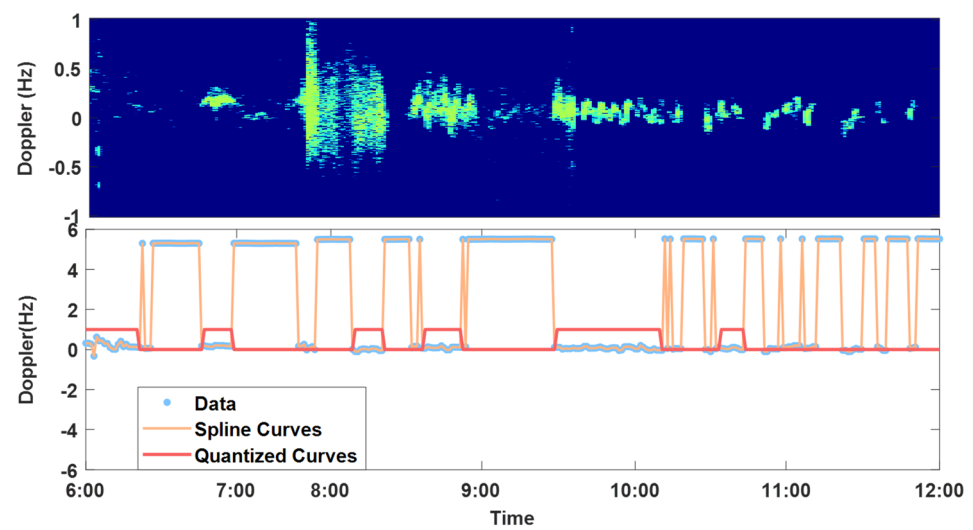
Figure 12. The results when the typhoon entered radar's detection range.
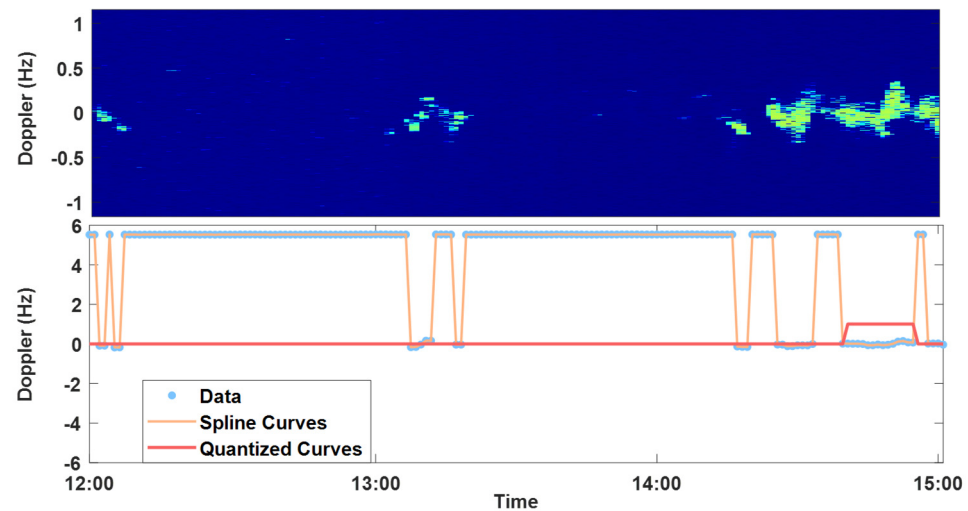
Figure 13. The results when the typhoon exited radar's detection range.

In addition, for the extracted first-order oceanic echoes, we calculate the value of R using Equation (2), selecting the middle point of the leftmost beam for analysis. By applying Gaussian smoothing to the raw data (as shown in Figure 14, where the blue line shows the original data and the orange line denotes the smoothed curve), and considering the characteristics of R, we identify the last minimum point as the critical inflection point. This point corresponds to the moment when the typhoon eye started entering the radar detection range (at 8:05), which serves as a key time for monitoring and analyzing typhoon activities. In addition, the results also match the typhoon track shown in Figure 7. Consequently, we label the time before 8:05 as "0" and the time thereafter as "1", with the red line indicating the corresponding disturbance detection results.
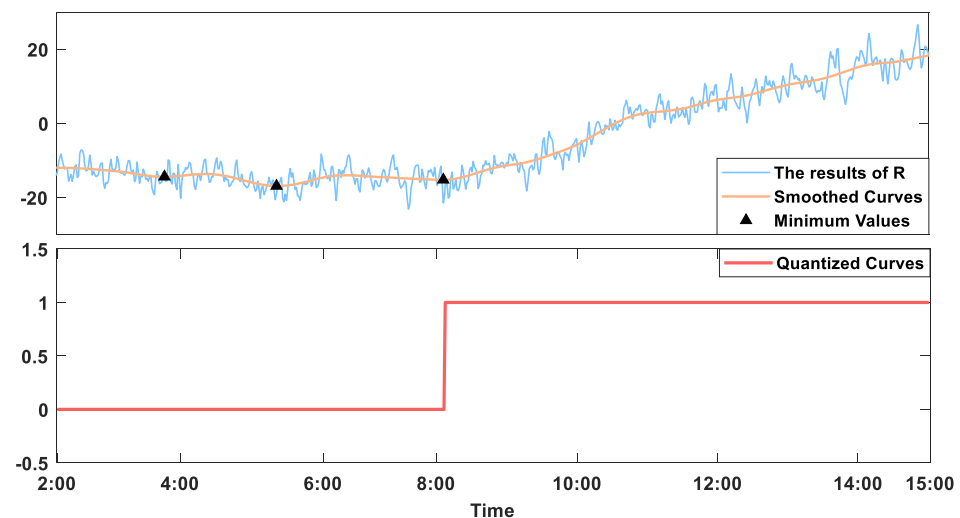
Figure 14. The results of the first-order peak energy ratio.

At last, Figure 15 presents the final outcomes of the typhoon early warning and monitoring, comprehensively utilizing ionospheric and oceanic echoes acquired through HFSWR. The results indicate that the ionospheric disturbance is detectable around 2:00, initiating the typhoon warning process, whereas the ocean surface disturbance emerges around 8:05, suggesting that the typhoon eye has entered the radar detection range, transitioning into the real-time typhoon monitoring stage. Compared to the typhoon path, the AGWs caused by typhoons outside radar detection range can propagate into the ionospheric region within detection range and result in TIDs, providing an estimated six-hour advance

in early warning. Consequently, employing the proposed scheme for early warning of typhoons and other anomalous sea conditions proves to be practical and effective.
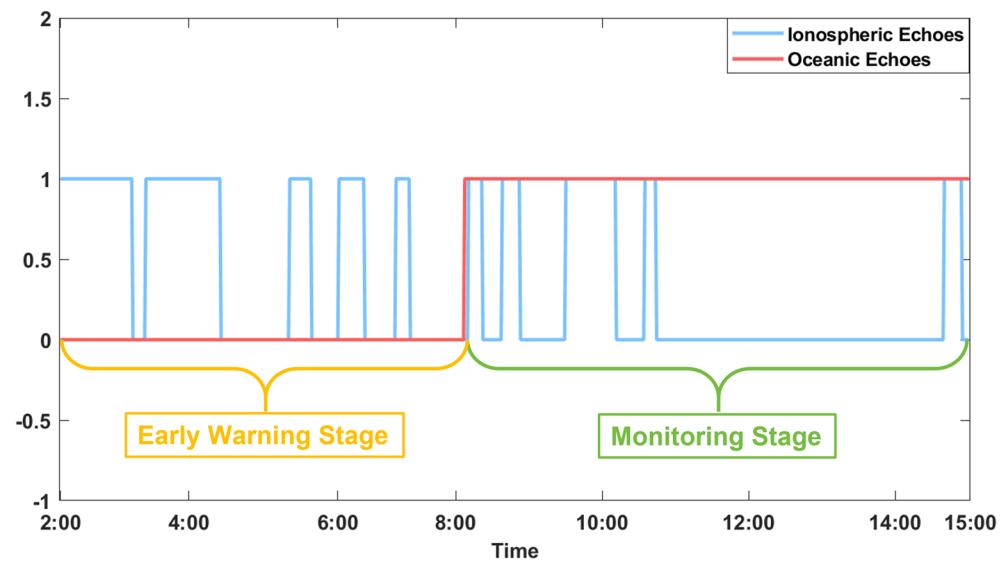
Figure 15. The disturbance detection results of ionospheric and sea echoes based on HFSWR.

5. Conclusions

After investigating and simulating the interaction processes about Typhoon-AGWs-Ionosphere and Typhoon-Ocean Waves for HFSWR, we developed a comprehensive early warning and monitoring scheme for typhoons that incorporates the characteristics of ionospheric and oceanic echoes. In addition, the workflow consists of four major steps: acquiring the measured data by HFSWR, extracting the echoes, extracting the parameters, and detecting the disturbances. Furthermore, the scheme was applied to deal with and analyze the measured data of Typhoon Muifa observed by HFSWR. The results reveal that approximately 6 hour prior to Typhoon Muifa entering the radar detection range, a distinct S-shaped TFD of ionospheric echoes was evident in non-typhoon areas, which can serve as effective early warning signals. In addition, at around 8:05, an increasing trend in the energy ratio of the first-order spectrum of oceanic echoes was noted, indicating the approach of the typhoon eye into the detection range, which aligns closely with the official typhoon path. The proposed scheme leverages the extensive and all-weather detection capabilities of HFSWR, which can offer reliable technical support for typhoon early warning and monitoring.

However, the inherent multi-scale and varying intensity characteristics of typhoons, along with environmental factors such as geographical location and topography, introduce significant uncertainties in their impact on the ionosphere and ocean waves. Therefore, future research should focus on further validating the universality of the proposed scheme by analyzing additional typhoon data. Moreover, exploring the integration of multi-site data and collaboration with other ionospheric monitoring techniques will also be a key focus of our future work, contributing to a more reliable early warning and monitoring system.

Author Contributions: Conceptualization, methodology, software, validation, formal analysis, data curation, writing—original draft preparation, writing—review and editing, visualization: M.J.; methodology, writing—review and editing, supervision, project administration, funding acquisition: Y.J.; methodology, software, writing—review and editing: R.Q.; software, investigation: H.Z.; resources, writing—review and editing J.D. All authors have read and agreed to the published version of the manuscript.

References

1. Gong, Z.; Ke, H.; Wu, X.; Cheng, F. HF Radar Observation of Longwang Typhoon in the Taiwan Straight. *Chin. J. Geophys.* **2007**, *50*, 1695–1702. (In Chinese)
2. Li, L.; Wu, X.; Li, Y.; Long, C.; Liu, B.; Xu, X.; Chen, M.; Xue, C. Ocean Surface Wind and Wave Monitoring at Typhoon Fung-Wong by HFSWR OSMAR071. *Yaogan Xuebao—J. Remote Sens.* **2021**, *16*, 154–165. [CrossRef]
3. Shen, Z.; Wu, X.; Cheng, X.; Xu, X. Complex EOF Analysis of Ocean Surface Currents Response to the Severe Tropical Storm Lionrock Measured with High Frequency Surface Wave Radar. In Proceedings of the OCEANS 2014, Taipei, Taiwan, 7–10 April 2014; pp. 1–4.
4. Li, Z.; Cao, H.; Jia, C. Observation of Wind Field in the Beibu Gulf during Typhnoon Usagi. *J. Trop. Oceanogr.* **2016**, *35*, 31–34. (In Chinese) [CrossRef]
5. Lai, J.; Wang, Y.; Yang, W.; Huang, C.; Chen, S.; Lin, K.; Kao, C.; Tang, S. Wind Direction Estimated from SeaSonde HF Radar during Typhoon Songda. In Proceedings of the 2012 Oceans, Yeosu, Republic of Korea, 21–24 May 2012; pp. 1–4.
6. Li, C.; Li, H.; Wang, H.; Gao, J.; Wang, G.; Dong, J.; Pan, S.; Liu, K. Data Analysis of High Frequency Surface Wave Radar at Zhujiajian-Shengshan during Typhoon Chan-hom. *J. Mar. Sci.* **2017**, *35*, 41–46. (In Chinese)
7. Xu, Q.; Wu, X.; Zhou, H.; Chen, Z.; Wan, Y.; Huang, Q.; Yue, X. Observation of Typhoon "Moranti" Eye with OSMAR071G. *J. Ocean Technol.* **2017**, *36*, 99–103. (In Chinese)
8. Zhou, H.; Wu, X.; Yue, X. Observation of Typhoon Meranti with High Frequency Radar System. In Proceedings of the IGARSS 2019–2019 IEEE International Geoscience and Remote Sensing Symposium, Yokohama, Japan, 28 July–2 August 2019; pp. 8129–8131.
9. Xie, X.; Wu, Y.; Liu, H.; Zhou, W. Data Verification of High Frequency Ground Wave Radar and Its Application in Typhoon Monitoring. *Radar ECM* **2020**, *40*, 43–48. (In Chinese) [CrossRef]
10. Song, Q.; Ding, F.; Zhang, X.; Liu, H.; Mao, T.; Zhao, X.; Wang, Y. Medium-Scale Traveling Ionospheric Disturbances Induced by Typhoon Chan- H Om Over China. *JGR Space Phys.* **2019**, *124*, 2223–2237. [CrossRef]
11. Bauer, S.J. An Apparent Ionospheric Response to the Passage of Hurricanes. *J. Geophys. Res.* **1958**, *63*, 265–269. [CrossRef]
12. Shen, C. The Correlations between the Typhoon and the f0F2 of Ionosphere. *Chin. J. Space Sci.* **1982**, *2*, 335–340. (In Chinese) [CrossRef]
13. Xiao, Z.; Xiao, S.; Hao, Y.; Zhang, D. Morphological Features of Ionospheric Response to Typhoon. *J. Geophys. Res.* **2007**, *112*, 2006JA011671. [CrossRef]
14. Li, Z.; Jia, C.; Huang, D. Research on Characteristics of Ionospheric Echo Based on Ocean. In Proceedings of the 2016 IEEE Advanced Information Management, Communicates, Electronic and Automation Control Conference (IMCEC), Xi'an, China, 3–5 October 2016; pp. 15–18.
15. Chung, Y.J.; Hung Chen, C.; Chen, Y.R.; Chiao Tsai, S.; Yang, Y.J.; Chuang, L.Z.H. Clutter Analysis of the Range-Doppler Spectra under the Influence of Typhoon. In Proceedings of the OCEANS 2019—Marseille, Marseille, France, 17–20 June 2019; pp. 1–5.
16. Hines, C.O. Internal Atmospheric Gravity Waves at Ionospheric Heights. In *The Upper Atmosphere in Motion*; American Geophysical Union (AGU): Washington, DC, USA, 1974; pp. 248–328, ISBN 978-1-118-66357-8.
17. Vanina-Dart, L.B.; Sharkov, E.A. Main Results of Recent Investigations into the Physical Mechanisms of the Interaction of Tropical Cyclones and the Ionosphere. *Izv. Atmos. Ocean. Phys.* **2016**, *52*, 1120–1127. [CrossRef]
18. Zhou, H.; Wen, B.; Wu, S. Time-Frequency Characteristics of the Ionospheric Clutters in High-Frequency Surface Wave Radars (in Chinese). *Chin. J. Radio Sci.* **2009**, *24*, 394–398. [CrossRef]
19. Zhou, H.; Wen, B.; Wu, S. Ionosphere Probing with a High Frequency Surface Wave Radar. *Prog. Electromagn. Res. C* **2011**, *20*, 203–214. [CrossRef]
20. Chen, S.; Huang, W.; Gill, E.W. First-Order Bistatic High-Frequency Radar Power for Mixed-Path Ionosphere-Ocean Propagation. *IEEE Geosci. Remote Sens. Lett.* **2016**, *13*, 1940–1944. [CrossRef]
21. Lyu, Z.; Yu, C.; Yao, D.; Liu, A.; Yang, X. Gravity Wave Observation Experiment Based on High Frequency Surface Wave Radar. *IEICE Trans. Fundam.* **2021**, *E104.A*, 1416–1420. [CrossRef]
22. Chen, X.; Yang, H.; Lyu, Z.; Yu, C. Chaotic Properties of Gravity Waves during Typhoons Observed by HFSWR. *Remote Sens.* **2023**, *15*, 5235. [CrossRef]

23. Wang, R.; Lyu, Z.; Yu, C.; Liu, A.; Quan, T. Joint Analysis and Morphological Characterization of HFSWR Echo Properties during Severe Typhoon Muifa. *Remote Sens.* **2024**, *16*, 267. [CrossRef]

24. Wang, R.; Lyu, Z.; Yu, C.; Liu, A.; Quan, T. Characterization of HFSWR Ocean-Ionospheric Response with Joint Gravity Wave Features Based on Dual-Coupled Duffing Oscillator. *IEEE Geosci. Remote Sens. Lett.* **2024**, *21*, 1–5. [CrossRef]

25. Heron, M.; Rose, R. On the Application of HF Ocean Radar to the Observation of Temporal and Spatial Changes in Wind Direction. *IEEE J. Ocean. Eng.* **1986**, *11*, 210–218. [CrossRef]

26. Zhang, S. Study on High Frequency Radar Ocean Surface Scattering and Remote Sensing. Ph.D. Thesis, Wuhan University, Wuhan, China, 2017. (In Chinese).

27. Ogunsua, B.O.; Srivastava, A.; Bian, J.; Qie, X.; Wang, D.; Jiang, R.; Yang, J. Significant Day-Time Ionospheric Perturbation by Thunderstorms along the West African and Congo Sector of Equatorial Region. *Sci. Rep.* **2020**, *10*, 8466. [CrossRef]

28. Barrick, D. First-Order Theory and Analysis of MF/HF/VHF Scatter from the Sea. *IEEE Trans. Antennas Propagat.* **1972**, *20*, 2–10. [CrossRef]

29. Hasselmann, D.E.; Dunckel, M.; Ewing, J.A. Directional Wave Spectra Observed during JONSWAP 1973. *J. Phys. Oceanogr.* **1980**, *10*, 1264–1280. [CrossRef]

30. Lipa, B.; Nyden, B. Directional Wave Information from the SeaSonde. *IEEE J. Ocean. Eng.* **2005**, *30*, 221–231. [CrossRef]

31. Fritts, D.C.; Lund, T.S. Gravity Wave Influences in the Thermosphere and Ionosphere: Observations and Recent Modeling. In *Aeronomy of the Earth's Atmosphere and Ionosphere*; Abdu, M.A., Pancheva, D., Eds.; Springer Netherlands: Dordrecht, The Netherlands, 2011; pp. 109–130. ISBN 978-94-007-0325-4.

32. Kherani, E.A.; Lognonné, P.; Hébert, H.; Rolland, L.; Astafyeva, E.; Occhipinti, G.; Coïsson, P.; Walwer, D.; De Paula, E.R. Modelling of the Total Electronic Content and Magnetic Field Anomalies Generated by the 2011 Tohoku-Oki Tsunami and Associated Acoustic-Gravity Waves: Ionospheric Anomalies/Tohoku Tsunami. *Geophys. J. Int.* **2012**, *191*, 1049–1066. [CrossRef]

33. Kherani, E.A.; Lognonné, P.; Kamath, N.; Crespon, F.; Garcia, R. Response of the Ionosphere to the Seismic Trigerred Acoustic Waves: Electron Density and Electromagnetic Fluctuations. *Geophys. J. Int.* **2009**, *176*, 1–13. [CrossRef]

34. Li, W.; Yue, J.; Wu, S.; Yang, Y.; Li, Z.; Bi, J.; Zhang, K. Ionospheric Responses to Typhoons in Australia during 2005–2014 Using GNSS and FORMOSAT-3/COSMIC Measurements. *GPS Solut.* **2018**, *22*, 61. [CrossRef]

35. Song, R.; Hattori, K.; Zhang, X.; Liu, J. The Two-Dimensional and Three-Dimensional Structures Concerning the Traveling Ionospheric Disturbances Over Japan Caused by Typhoon Faxai. *JGR Space Phys.* **2022**, *127*, e2022JA030606. [CrossRef]

36. Yang, X.; Wang, M.; Huang, W.; Yu, C. Experimental Observation and Analysis of Ionosphere Echoes in the Mid-Latitude Region of China Using High-Frequency Surface Wave Radar and Ionosonde. *IEEE J. Sel. Top. Appl. Earth Obs. Remote Sens.* **2020**, *13*, 4599–4606. [CrossRef]

37. Yang, X.; Liu, A.; Yu, C.; Wang, L. Ionospheric Clutter Model for HF Sky-Wave Path Propagation with an FMCW Source. *Int. J. Antennas Propag.* **2019**, *2019*, 1782942. [CrossRef]

38. Chernogor, L.F. A Tropical Cyclone or Typhoon as an Element of the Earth–Atmosphere–Ionosphere–Magnetosphere System: Theory, Simulations, and Observations. *Remote Sens.* **2023**, *15*, 4919. [CrossRef]

39. Zhao, Y.; Deng, Y.; Wang, J.; Zhang, S.; Lin, C.Y. Tropical Cyclone-induced Gravity Wave Perturbations in the Upper Atmosphere: GITM-R Simulations. *JGR Space Phys.* **2020**, *125*, e2019JA027675. [CrossRef]

40. Ji, Y.; Zhang, J.; Wang, C.; Chu, X.; Wang, Y.; Yang, L. First-order Sea Clutter Spectrum Extraction Based on SNR Method for HF Hybrid Sky-surface Wave Radar. *J. Electron. Inf. Technol.* **2015**, *37*, 2177–2182.

41. Otsu, N. A Threshold Selection Method from Gray-Level Histograms. *IEEE Trans. Syst. Man Cybern.* **2007**, *9*, 62–66. [CrossRef]